White Rose Research Online

eprints@whiterose.ac.uk
https://eprints.whiterose.ac.uk
Universities of Leeds, Sheffield and York

Deposited via The University of Leeds.

White Rose Research Online URL for this paper:
https://eprints.whiterose.ac.uk/id/eprint/81766/

Version: Published Version

Article:
Liang, G, Dupont, E, Fathololoumi, S et al. (2014) Planar integrated metasurfaces for highly-collimated terahertz quantum cascade lasers. Scientific Reports, 4. 7083. ISSN: 2045-2322

https://doi.org/10.1038/srep07083

Reuse
Items deposited in White Rose Research Online are protected by copyright, with all rights reserved unless indicated otherwise. They may be downloaded and/or printed for private study, or other acts as permitted by national copyright laws. The publisher or other rights holders may allow further reproduction and re-use of the full text version. This is indicated by the licence information on the White Rose Research Online record for the item.

Takedown
If you consider content in White Rose Research Online to be in breach of UK law, please notify us by emailing eprints@whiterose.ac.uk including the URL of the record and the reason for the withdrawal request.

UNIVERSITY OF LEEDS
University of Sheffield
UNIVERSITY of York

SCIENTIFIC REPORTS

OPEN

SUBJECT AREAS:
QUANTUM CASCADE LASERS
METAMATERIALS

Received
24 July 2014

Accepted
16 October 2014

Published
18 November 2014

Correspondence and requests for materials should be addressed to Q.J.W. (qjwang@ntu.edu.sg)

Planar integrated metasurfaces for highly-collimated terahertz quantum cascade lasers

Guozhen Liang[1], Emmanuel Dupont[2], Saeed Fathololoumi[2,3], Zbigniew R. Wasilewski[3], Dayan Ban[3], Hou Kun Liang[4], Ying Zhang[4], Siu Fung Yu[5], Lianhe H. Li[6], Alexander Giles Davies[6], Edmund H. Linfield[6], Hui Chun Liu[7] & Qi Jie Wang[1]

[1]School of Electrical and Electronic Engineering, Nanyang Technological University, 50 Nanyang Avenue, 639798, Singapore, [2]National Research Council, Bldg. M-50, 1200 Montreal Rd, Ottawa, Ontario K1A0R6, Canada, [3]Department of Electrical and Computer Engineering, Waterloo Institute for Nanotechnology, University of Waterloo, 200 University Ave. West, Waterloo, Ontario N2L3G1, Canada, [4]Singapore Institute of Manufacturing Technology, 71 Nanyang Drive, 638075, Singapore, [5]Department of Applied Physics, Hong Kong Polytechnic University, Kowloon, Hong Kong, [6]School of Electronic and Electrical Engineering, University of Leeds, Leeds LS2 9JT, UK, [7]Key Laboratory of Artificial Structures and Quantum Control, Department of Physics, Shanghai Jiao Tong University, Shanghai 200240, China.

We report planar integration of tapered terahertz (THz) frequency quantum cascade lasers (QCLs) with metasurface waveguides that are designed to be spoof surface plasmon (SSP) out-couplers by introducing periodically arranged SSP scatterers. The resulting surface-emitting THz beam profile is highly collimated with a divergence as narrow as ~4° × 10°, which indicates a good waveguiding property of the metasurface waveguide. In addition, the low background THz power implies a high coupling efficiency for the THz radiation from the laser cavity to the metasurface structure. Furthermore, since all the structures are in-plane, this scheme provides a promising platform where well-established surface plasmon/metasurface techniques can be employed to engineer the emitted beam of THz QCLs controllably and flexibly. More importantly, an integrated active THz photonic circuit for sensing and communication applications could be constructed by incorporating other optoelectronic devices such as Schottky diode THz mixers, and graphene modulators and photodetectors.

Surface plasmons (SPs) are surface electromagnetic waves bound at the interface between metallic and dielectric materials. A flexible means of confining or manipulating optical waves at a subwavelength level can thus be achieved by patterning the metallic surface, and as such SPs have underpinned numerous studies on compact photonic circuits[1], enhanced light-matter interactions[2], near-field imaging systems[3,4], and beam shaping[5–7], *inter alia*. Conventionally, operation of these plasmonic devices relies on external illumination of a properly polarized laser beam on an input coupler (such as a prism or grating), where the SPs are generated. However, these methods often require meticulous alignment of the external optical components, which are bulky and inconvenient for compact integration. Therefore, efforts have been made to integrate plasmonic structures monolithically with semiconductor lasers, resulting in integrated active plasmonic devices. As a straightforward implementation, various kinds of plasmonic structures have been integrated directly onto semiconductor laser facets for beam shaping, such as generating deep-subwavelength laser spots[8,9], reducing beam divergence[6,10], producing multi-beam emissions[11,12], and controlling the polarization state[13]. Moreover, integration of a passive SP waveguide into a semiconductor laser has also been recently demonstrated[14,15].

Although the use of SPs in these types of devices has proven successful in the visible to mid-infrared regions of the spectrum, the SP concept cannot be easily translated into the terahertz (THz) region. This is because the metal behaves more like a perfect conductor at such frequencies, and hence the penetration depth of the THz field into the metal is negligible (three orders of magnitude shorter than the wavelength in free space); this leaves the electromagnetic field only loosely bound to the flat surface. However, it was found that artificial metallic structures at a deep-subwavelength scale can mimic the optical response of the metal atoms to visible and near-infrared light in the longer wavelength region. Metasurface made from such 'artificial atoms' (meta-atoms) can thus been designed to support tightly confined THz surface waves[16–19] in a way just like the SP behavior of metal at shorter wavelengths. Moreover, the dispersion relation of these THz surface waves, usually referred to as 'spoof' surface

plasmons (SSPs), can be geometrically tailored, providing additional freedom in the design of THz plasmonic devices.

The invention of the THz frequency quantum cascade laser (QCL)[20] in 2002 opened up a number of possibilities for THz photonics[21–23]. THz QCLs are electrically pumped compact semiconductor lasers based on the electronic transitions between subbands in the conduction band, which can be flexibly engineered. As such, the light in the active region is intrinsically TM-polarized, matching the polarization of SPs. Therefore, QCLs are potentially ideal sources for integrated THz active plasmonic system. For example, using a planar-integrated metasurface waveguide, it is possible to couple the THz radiation directly and efficiently out of the laser cavity as SSP waves, which can then be fed into a SSP device or circuit. Although an integrated THz metasurface collimator has been demonstrated on a QCL facet itself[23], the fabrication was difficult, requiring use of focused ion beam technology, and the small facet area also limits its adoption for practical applications. Planar integration of metasurface components to a THz source for active plasmonic systems has yet to be demonstrated.

In this letter, we report the planar integration of tapered THz QCLs with metasurface structures, which are processed into SSP out-couplers by introducing periodically arranged scatterers. The resulting surface-emitting THz beam is highly collimated with a beam divergence as narrow as $\sim 4^\circ \times 10^\circ$. This low divergence indicates a good waveguiding property of the metasurface waveguide, and the low background THz power, away from the surface-emitting beam, implies a high coupling efficiency of the THz radiation from the laser cavity to the metasurface. Moreover, since the whole structure is in-plane, this scheme provides a promising platform where well-established surface plasmon techniques can be employed to engineer an emitted THz QCL beam controllably and flexibly. Furthermore, an integrated active THz photonic circuit may be constructed by guiding and coupling the SSP to other optoelectronic devices such as a Schottky diode THz mixer[21,22], or graphene modulators[24] and photodetectors[25].

Results and discussion

Figure 1(a) shows a scanning electron microscope image of a fabricated device, where the tapered THz QCL is shown on the left and the metasurface structure on the right. The laser cavity is formed between the curved facet of the tapered structure and a back distributed Bragg reflector (DBR) towards the left of the ridge region (inset of Figure 1(a)). The metasurface structure consists of a SSP waveguide (periodic narrow and shallow gold-coated grooves, each of which functions as a simple one-dimensional meta-atom) and SSP scatterers (wide and deep gold-coated grooves), as illustrated in Figure 1(b), which is a 3D schematic cross-sectional view of the device along the white dashed line in Figure 1(a). Figure 1(c) then presents an enlarged top view of the central region of Figure 1(a), showing details of the fabricated device.

Design of the tapered laser cavity. The tapered THz QCL used in this work comprises a 10-μm-thick active region design, labeled as V775 with a gain peak at ~3 THz (~100 μm)[26]; this is confined by a double-metal waveguide structure in the vertical (*z*-) direction. The QCL is patterned with a tapered structure, first to collimate the emission in the lateral direction as the ideal input for the one-dimensional SSP waveguide is a parallel beam (the beam divergence in the lateral direction is inversely proportional to the facet width) and, second, to increase the THz emission amplification in the laser cavity. Figure 2(a) shows a numerical simulation of the electric field (E_z) distribution of the tapered THz QCL calculated using COMSOL Multiphysics, a commercial finite-element-method solver. The taper section has a tapering angle of ~36° and a length of 800 μm, which increases the width of the output facet from 50 μm to 500 μm. The shape of the taper facet is designed to be an arc centered 20 μm to the left of the ridge-taper interface to collimate the output beam (Figure 2(a)). A flat taper facet[27] is not appropriate for such a large tapering angle because it significantly distorts the optical field owing to the large mismatch between the shape of the facet and the wavefront of the radiation emitted from the laser ridge, which would lead to an uncollimated emitted beam (Figure 2(b)). The rear DBR (Figure 2(a)) is simply formed by a metal grating patterned on top of the active region. Finally, to suppress higher-order lateral modes, side-absorbers (black regions in Figures 2(a) and (b)) are created by leaving the active region uncovered by the metal; the exposed upper n^+-GaAs contact layer of the active region acts as an efficient absorber with which the higher-order lateral modes have

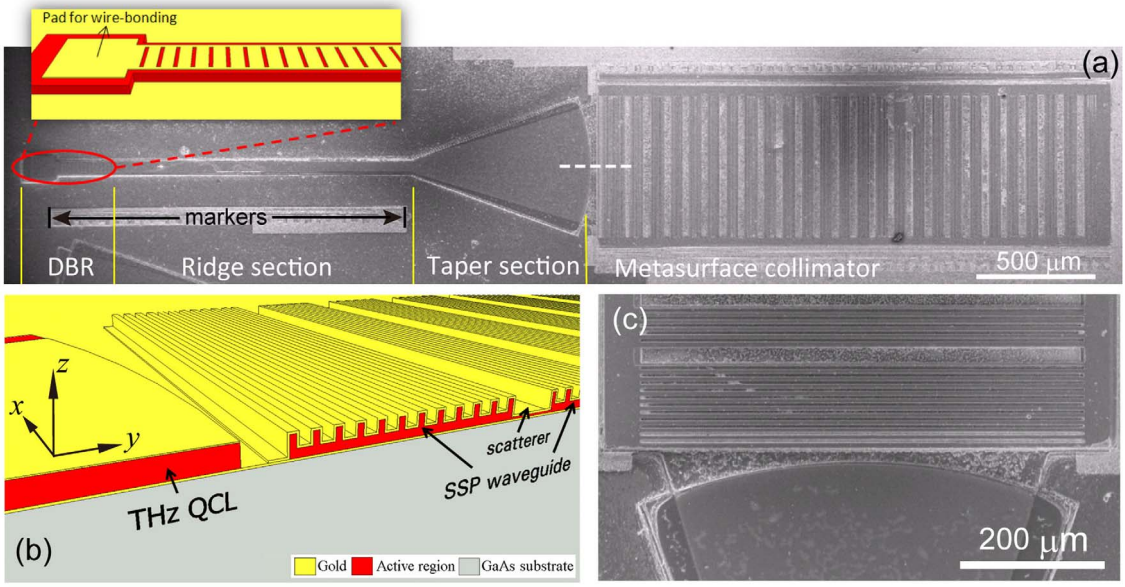

Figure 1 | (a) Scanning electron microscope (SEM) image of a fabricated device. The tapered THz QCL consists of DBR, ridge and taper sections. The inset shows the details of the DBR structure, which is formed simply by gold patterning on top of the active region. The markers by the side of the laser are used for mask alignment during the fabrication. (b) 3D schematic cross-sectional view of the device along the white dashed line in (a). (c) Enlarged top view of the central region of the device.

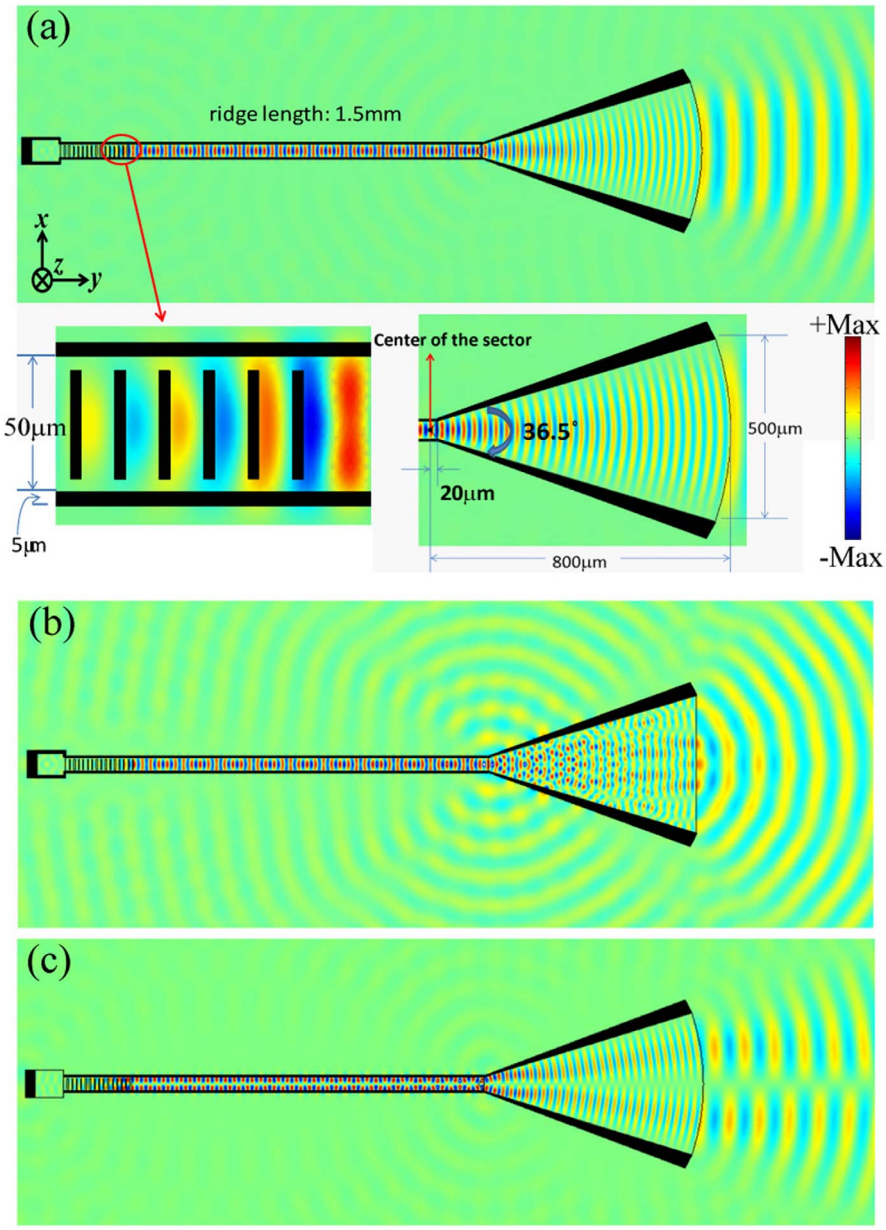

Figure 2 | (a) Electric field (E_z) distribution of the tapered THz QCL with a curved front facet; magnified views show the details of the DBR region, and the taper. The black regions represent the active regions without metal coverage, which are highly absorbing. (b) E_z distribution of a tapered structure with a flat facet. The electric field in the laser cavity is distorted, resulting in uncollimated emission. (c) E_z distribution of a second-order lateral mode which is suppressed due to a larger overlap of the mode with the side absorbers.

larger overlaps than the fundamental lateral mode[28]. Figure 2(c) shows the electric field distribution of a second-order lateral mode of the structure.

Design of the metasurface collimator. Figure 3(a) shows a 2D simulation of the electric field distribution of the whole device performed in the y-z plane along the symmetric line of the structure (white dashed line in Figure 1(a)), with the metasurface collimator geometry presented in Figure 3(b). The excitation and scattering of the SSPs can be clearly observed. The SSP wavelength varies from 89.4 μm to 92.7 μm as the wave propagates away from the laser facet, compared to a 96 μm value in free space. The shorter SSP wavelength in the vicinity of the laser facet is explained by a larger wavevector of the orange region than that of the yellow region in Figure 3(b), as reflected in the dispersion diagram (Figure 3(c)), which was obtained by a finite-difference time-domain (FDTD) method with the commercial Lumerical software. The SSP dispersions show strong similarities with the dispersion of the SP mode on a flat metal surface. However, while the asymptotic frequency f_c of the SP mode is fixed as $\omega_p/2\sqrt{2}\pi$ (ω_p is the bulk plasma frequency of the metal), f_c of this groove-type metasurface and thus the behavior of the SSP mode, can be controlled by the groove depth h: $f_c \approx c_0/4h$,[19] where c_0 is the velocity of light in vacuum. For a given frequency, a smaller asymptotic frequency means a larger SSP wavevector, which implies a better confinement of the surface wave. Nevertheless, a stronger confinement of wave on metal surface comes with a larger ohmic loss in the metal. Therefore, tradeoff should be made between the confinement and propagation length in practice.

In Figure 3(a), the 1/e evanescent tail of the SSP wave is around 50 μm, in agreement well with the value calculated by $1/\sqrt{k_{ssp}^2 - k_0^2}$, with k_{ssp} being the SSP wave vector and k_0 the free-space wave vector.

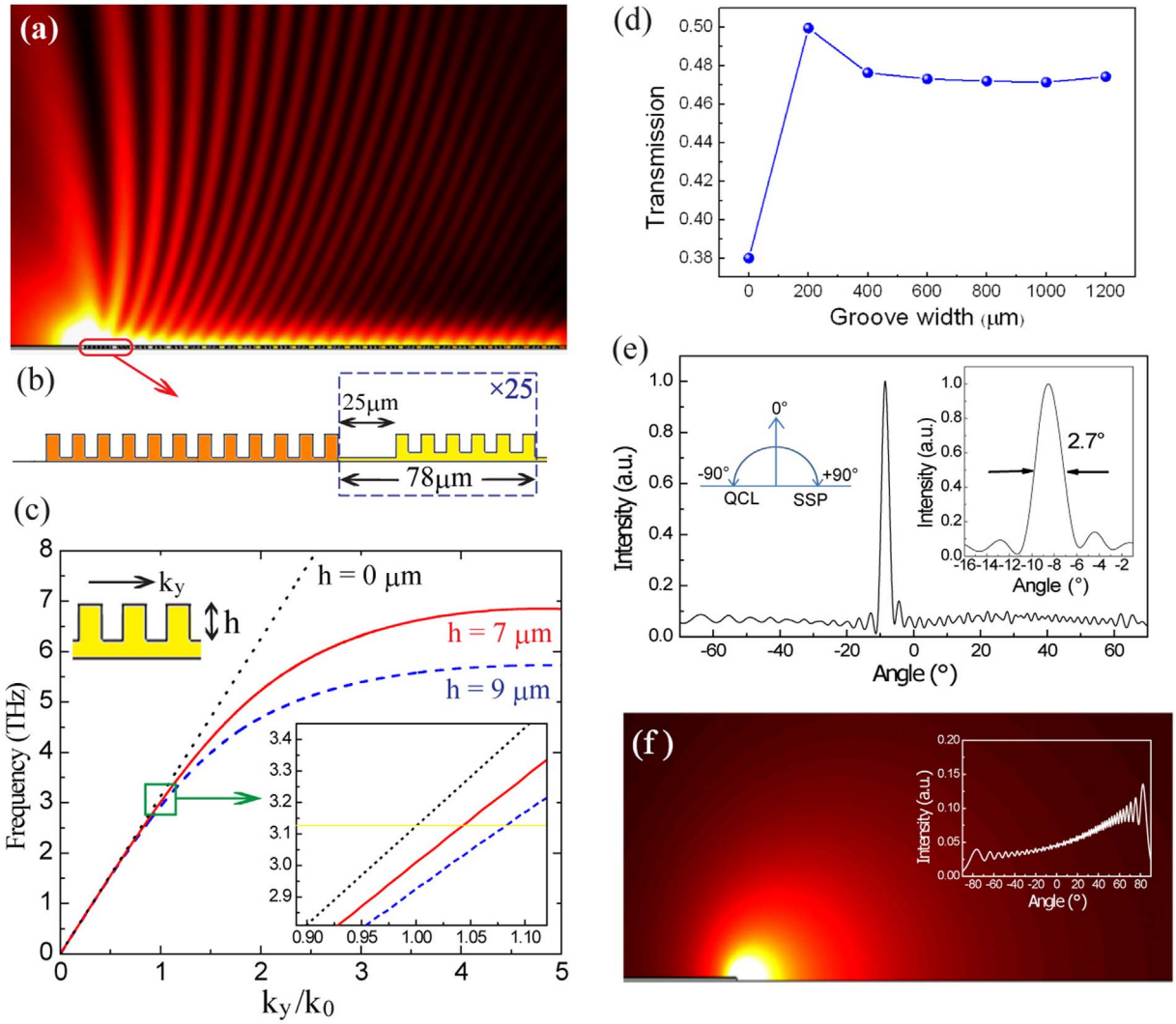

Figure 3 | (a) Simulated 2D light intensity distribution of a metasurface collimator. The simulation was performed in the (y-z) plane along the symmetric line (white dashed line in Figure 1(a)) of the device. (b) Cross-section of the metasurface collimator design. The narrow grooves have a width of 5 μm and a period of 10 μm. The narrow grooves are 9 μm deep in the orange region and 7 μm deep in the yellow region (which is repeated 25 times). The narrow grooves in the orange region are deeper to enhance coupling from the laser into the SSPs. The 25 μm grooves, which scatter out the SSPs, are 9 μm in depth. (c) Dispersion diagrams of the metasurface with grooves of 5 μm width and 10 μm period, but different depths. The black dotted curve, red curve and the blue dashed curve correspond to h = 0 μm (flat surface), 7 μm and 9 μm, respectively. The h = 0 μm curve almost coincides with the light line in vacuum in the THz frequency range. The lower inset presents a zoom-in view of the region marked by a green box. (d) Dependence of the transmission through the laser facet on the width of the metasurface. (e) Calculated far-field intensity profile along the metasurface waveguide direction. The enlarged view of the central lobe in the inset shows that the beam divergence is as narrow as 2.7°. (f) Simulated 2D light intensity of a laser without the metasurface structure. The inset shows that the light emission is relatively uniform in all directions.

The corresponding ohmic loss of the metal is 1–2 cm^{-1}. With respect to the emission power, it is dependent on the intensity transmission at the laser output facet, which can be expressed as $T = 1 - \left|\frac{Z_F - Z_{MM}}{Z_F + Z_{MM}}\right|^2$, where Z_{MM} and Z_F are the impedance of the QCL's metal-metal waveguide and that of the outer space seen from the laser facet, respectively. Usually, Z_F is much larger than Z_{MM} (large impedance mismatch), resulting in an insufficient output efficiency of the THz power. However, Z_F is affected by the surrounding environment of the laser facet. In our case here, the metasurface varies Z_F in such a way as to reduce the mismatch between Z_F and Z_{MM}, leading to a higher output power. With this in mind, it is logical that the width of the metasurface might have effect on the facet transmission. However, if the grooves of the metasurface is wide enough to cover the entire width of the laser facet (500 μm), the transmissions through the laser facet are almost the same with an enhancement factor of ~1.2 compared to the case without metasurface (Figure 3(d)). In terms of coupling efficiency, it is estimated that 40% of the laser output power is coupled into the SSPs, with the remaining radiated directly into free space. Most of the power in the SSPs is then scattered out perpendicular to the device surface (z-direction) by the 25 SSP scatterers, which are grooved on the waveguide with a periodicity of 78 μm so that the scattered SSP light and the uncoupled light interfere constructively, resulting in a narrow (~3°) single lobe in the far field (Figure 3(d)). As a comparison, the laser without the metasurface structure emits uniformly in all directions, as shown in Figure 3(e).

Light-current-voltage and far-field characterization. Devices with two different groove widths were fabricated, labeled as A and B. The groove widths of device A were 600 μm, whilst device B had a wider groove width of 1000 μm. Both devices show similar light-current-voltage (LIV) characteristics. Figure 4 shows the LIV curves of a typical device as a function of temperature; the insets show the

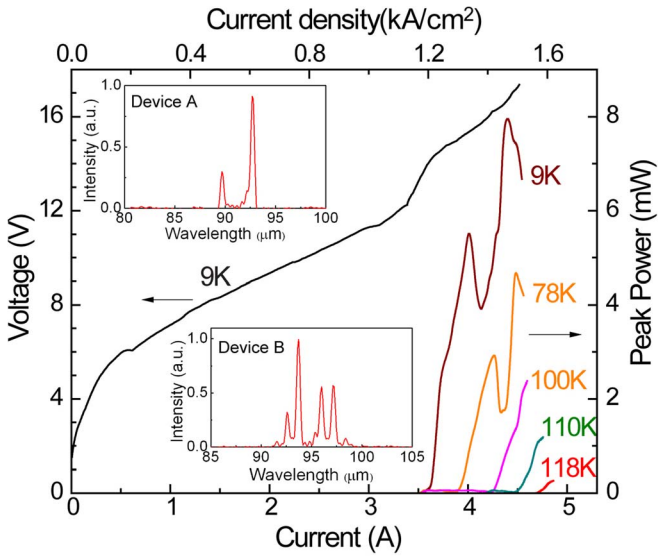

Figure 4 | Pulsed light-current-voltage (LIV) characteristics of device A (see Figure 5(a)) at different heat sink temperatures. Inset: Lasing spectra of devices A and B at 4.3 A and 9 K – conditions under which their far-field emission profiles were measured.

lasing spectra of devices A and B at 4.3 A and a 9 K heat sink temperature, the conditions at which their far field emission profiles were measured. The maximum operating temperature was found to be around 118 K under pulse mode operation with a 500 ns pulse width and 10 kHz repetition rate, comparable with that of a ridge laser (100 μm wide and 1500 μm long) fabricated from the same QCL active region, which operated up to 136 K under the same pulsing conditions.

2D far-field emission patterns of the devices were measured by scanning a pyroelectric detector on a spherical surface centered on the curved laser facet. 3D simulations were also performed using Lumerical FDTD. Figure 5(c) shows the measured far-field pattern of device A, with Figure 5(b) showing the line scans through the peak value. This reveals that the beam divergence in the φ direction is as low as ~4°, while it is ~10° in the θ direction. Moreover, the background intensity is less than 10% of the peak value, indicating a high coupling efficiency of the THz radiation into the SSPs. Note that the measured beam divergence in the φ direction is larger than the simulated results at a wavelength of 94 μm (Figure 5(e)). This is due to the multi-mode emission of the devices (inset of Figure 4) – the position of the radiation lobe shifts in the φ direction in the far-field as the laser wavelength changes. Simulations show that a change of 1 μm in the wavelength leads to ~1° shift in the far-field pattern. Therefore, the measured far-field pattern is actually the superimposition of several slightly shifted far-field patterns if the device is not operating single-mode. This effect is more apparent for device B, which has a wider emission spectrum (inset of Figure 4). The measured and simulated far-field patterns of device B are shown in Figures 5(d) and (f), respectively. Here, the simulation considered the emission bandwidth from 92 μm to 98 μm, and closer agreement is obtained.

Influence of the groove width on the far fields. In contrast to our original expectation that device B would gives a narrower beam divergence in the θ direction as it is with a wider groove width, it actually has a larger beam divergence in the θ direction than device A. To understand this phenomenon, we investigated the near-field distributions of the two devices (Figure 6(a) and (b)). The SP is found to spread in the lateral direction so that device B indeed provides a broader laser emission width compared with device A. However, the spread of the SSP in the lateral direction induces phase delays of the electric field. Figures 6(c) and (d) plot the amplitude and phase distributions of the radiative electric field (E_y) along the white

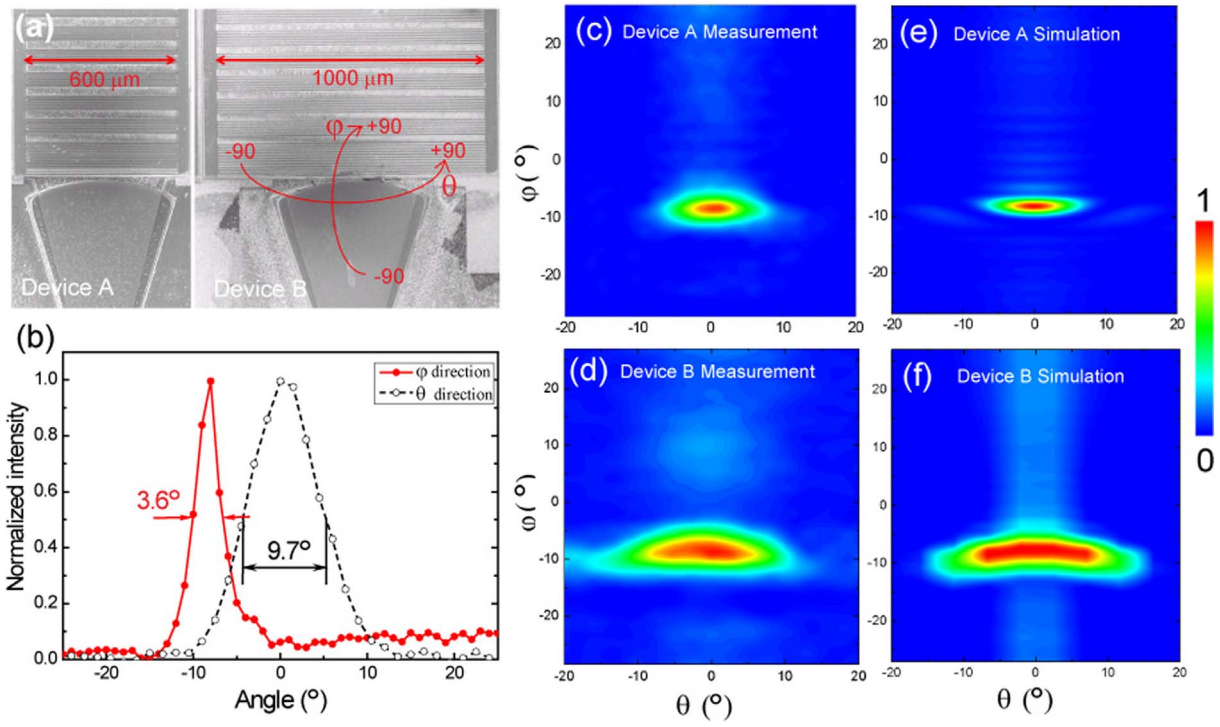

Figure 5 | (a) SEM images of device A and B with groove widths of 600 μm and 1000 μm, respectively. (b) φ and θ direction line scans through the peak in the measured far-field radiation pattern in (c) for device A. (c) and (d) Measured far-field patterns of devices A and B, respectively. (e) Simulated far-field pattern of device A at the wavelength of 94 μm. (f) Simulated far-field patterns of device B taking into consideration the multi-mode emission from the active region at wavelengths between 92 μm and 98 μm.

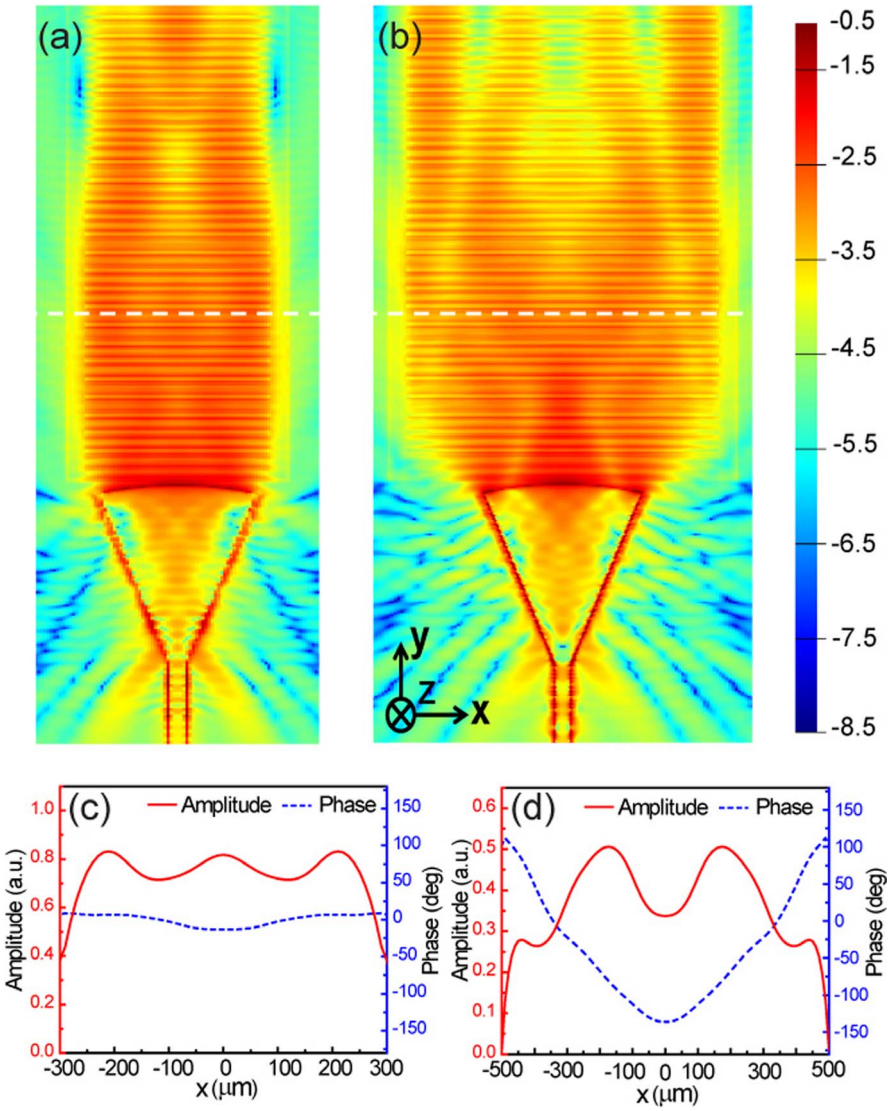

Figure 6 | Near field light intensity distributions of (a) device A and (b) device B on a logarithmic scale, taken on a plane 2 μm above the device surface. (c) and (d) Amplitude and phase distributions of the radiative electric field (E_y) along the white dashed line in (a) and (b), respectively.

dashed lines in Figures 6(a) and (b). As shown in Figure 6(c) and (d), the phase of E_y of device B varies greatly in the lateral (x-) direction, whereas it is almost uniform for device A. The large phase difference ($>180^\circ$) of the electric field between the central region and the lateral boundary region in device B leads to destructive interference in the far field, thereby giving a larger beam divergence.

Summary. In conclusion, we have demonstrated in-plane integration of THz tapered QCLs with metasurface waveguides. As an illustrative example, the metasurface waveguides were made into a plasmonic directional out-coupler for beam collimation of the generated THz wave from QCLs. The output beam is highly collimated with a beam divergence as narrow as $\sim 4^\circ \times 10^\circ$. Moreover, low background THz power (less than 10% of the peak value) indicates a high coupling efficiency of the light from the laser facet to the metasurface. We note that not only can the metasurface waveguides be processed into various geometries to shape the output emission profile, but they can also serve as a platform for integrated THz circuits for applications in sensing, spectroscopy, and communications.

Methods

Devices fabrication. Fabrication of the tapered THz QCLs with metasurface waveguides began with Au-Au thermocompression bonding of the QCL active region to an n+ GaAs receptor wafer. The original QCL substrate was then removed by a combination of lapping and selective chemical etching. A top contact metal (Ti/Au 15/350 nm) was next defined by conventional optical lithography and lift-off, the DBR section was also formed in the same process. The laser mesa and deep grooves (SPP scatterers) were first etched down ~3 μm by reactive ion etching (RIE) using a SiO_2 mask. Another lithography process was then performed to define additional patterns for the shallow grooves (SSP waveguide) on the same SiO_2 mask. The sample was subsequently etched again by RIE until the depth of the shallow grooves reached 7 μm. At this point, the 10-μm active region around the laser mesa and outside the metasurface was total removed while there remained 1 μm on the bottoms of the deep grooves. This was followed by (and without removing the SiO_2 mask) multiple-angle Ti/Au electron-beam evaporation to ensure full coverage of metal on the whole structure. The Ti/Au layer on the laser top and sidewalls was then removed by a gold etchant and a dilute HF solution with a thick AZ4620 photoresist covering the metasurface region. The SiO_2 mask on top of the laser was then removed by RIE using a mixture of HF_4 and O_2 gases. The substrate was thinned to 120 μm and a 20/300 nm Ti/Au layer deposited to form the bottom contact. The samples were cleaved, indium-mounted on Cu submounts, wire-bonded, and finally attached to the cold finger of a cryostat for measurement.

1. Ebbesen, T. W., Genet, C. & Bozhevolnyi, S. I. Surface-plasmon circuitry. *Phys. Today* **61**, 44 (2008).
2. Ng, B. *et al.* Spoof Plasmon Surfaces: A Novel Platform for THz Sensing. *Adv. Opt. Mater.* **1**, 543–548 (2013).
3. Huber, A. J., Keilmann, F., Wittborn, J., Aizpurua, J. & Hillenbrand, R. Terahertz near-field nanoscopy of mobile carriers in single semiconductor nanodevices. *Nano Lett.* **8**, 3766–70 (2008).

4. Luo, X. & Ishihara, T. Surface plasmon resonant interference nanolithography technique. *Appl. Phys. Lett.* **84**, 4780 (2004).
5. Li, L., Li, T., Wang, S., Zhang, C. & Zhu, S. Plasmonic Airy Beam Generated by In-Plane Diffraction. *Phys. Rev. Lett.* **107**, 1–4 (2011).
6. Lezec, H. J. *et al.* Beaming light from a subwavelength aperture. *Science* **297**, 820–2 (2002).
7. Yu, N., Wang, Q. J. & Capasso, F. Beam engineering of quantum cascade lasers. *Laser Photon. Rev.* **6**, 24–46 (2012).
8. Cubukcu, E., Kort, E. A., Crozier, K. B. & Capasso, F. Plasmonic laser antenna. *Appl. Phys. Lett.* **89**, 093120 (2006).
9. Guo, B., Song, G. & Chen, L. Plasmonic very-small-aperture lasers. *Appl. Phys. Lett.* **91**, 021103 (2007).
10. Yu, N. *et al.* Small-divergence semiconductor lasers by plasmonic collimation. *Nat. Photonics* **2**, 564–570 (2008).
11. Tetienne, J.-P. *et al.* Dipolar modeling and experimental demonstration of multi-beam plasmonic collimators. *New J. Phys.* **13**, 053057 (2011).
12. Yu, N. *et al.* Multi-beam multi-wavelength semiconductor lasers. *Appl. Phys. Lett.* **95**, 161108 (2009).
13. Yu, N. *et al.* Semiconductor lasers with integrated plasmonic polarizers. *Appl. Phys. Lett.* **94**, 151101 (2009).
14. Babuty, A. *et al.* Semiconductor Surface Plasmon Sources. *Phys. Rev. Lett.* **104**, 226806 (2010).
15. Schwarz, B. *et al.* Monolithically integrated mid-infrared lab-on-a-chip using plasmonics and quantum cascade structures. *Nat. Commun.* **5**, 4085 (2014).
16. Pendry, J., Holden, A., Stewart, W. & Youngs, I. Extremely low frequency plasmons in metallic mesostructures. *Phys. Rev. Lett.* **76**, 4773–4776 (1996).
17. Williams, C. R. *et al.* Highly confined guiding of terahertz surface plasmon polaritons on structured metal surfaces. *Nat. Photonics* **2**, 175–179 (2008).
18. Navarro-Cía, M. *et al.* Broadband spoof plasmons and subwavelength electromagnetic energy confinement on ultrathin metafilms. *Opt. Express* **17**, 18184–95 (2009).
19. Garcia-Vidal, F. J., Martín-Moreno, L. & Pendry, J. B. Surfaces with holes in them: new plasmonic metamaterials. *J. Opt. A Pure Appl. Opt.* **7**, S97–S101 (2005).
20. Köhler, R. *et al.* Terahertz semiconductor-heterostructure laser. *Nature* **417**, 156–159 (2002).
21. Wanke, M., Young, E. & Nordquist, C. Monolithically integrated solid-state terahertz transceivers. *Nat. Photonics* **4**, 565–569 (2010).
22. Hübers, H.-W. Terahertz technology: Towards THz integrated photonics. *Nat. Photonics* **4**, 503–504 (2010).
23. Yu, N. *et al.* Designer spoof surface plasmon structures collimate terahertz laser beams. *Nat. Mater.* **9**, 730–735 (2010).
24. Sensale-Rodriguez, B. *et al.* Broadband graphene terahertz modulators enabled by intraband transitions. *Nat. Commun.* **3**, 780 (2012).
25. Zhang, B. Y. *et al.* Broadband high photoresponse from pure monolayer graphene photodetector. *Nat. Commun.* **4**, 1811 (2013).
26. Fathololoumi, S. *et al.* Effect of oscillator strength and intermediate resonance on the performance of resonant phonon-based terahertz quantum cascade lasers. *J. Appl. Phys.* **113**, 113109 (2013).
27. Li, Y., Wang, J., Yang, N., Liu, J. & Wang, T. The output power and beam divergence behaviors of tapered terahertz quantum cascade lasers. *Opt. Express* **21**, 15998–16006 (2013).
28. Chassagneux, Y. *et al.* Electrically pumped photonic-crystal terahertz lasers controlled by boundary conditions. *Nature* **457**, 174–178 (2009).

Acknowledgments

This work is supported by grants funded by Ministry of Education, Singapore (MOE2011-T2-2-147 and MOE2011-T3-1-005). AGD and EHL acknowledge support of the EPSRC (UK), the EC programmes NOTES and TOSCA, the Royal Society and the Wolfson Foundation.

Author contributions

G.Z.L. and Q.J.W. conceived the idea, G.Z.L. completed the numerical simulations, devices fabrication, measurements, and carried out the data analyses and presentations. E.D., S.F., Z.R.W., D.B., H.C.L., L.H.Li, A.G.D. and E.H.L. performed the growth of the QCL active region. G.Z.L. and Q.J.W. wrote the manuscript. A.G.D., E.H.L., S.F.Y., H.K.L and Y.Z. improved the manuscript presentation. All authors reviewed the manuscript.

Additional information

Competing financial interests: The authors declare no competing financial interests.

How to cite this article: Liang, G. *et al.* Planar integrated metasurfaces for highly-collimated terahertz quantum cascade lasers. *Sci. Rep.* **4**, 7083; DOI:10.1038/srep07083 (2014).

This work is licensed under a Creative Commons Attribution-NonCommercial-ShareAlike 4.0 International License. The images or other third party material in this article are included in the article's Creative Commons license, unless indicated otherwise in the credit line; if the material is not included under the Creative Commons license, users will need to obtain permission from the license holder in order to reproduce the material. To view a copy of this license, visit http://creativecommons.org/licenses/by-nc-sa/4.0/